EasyChair Preprint

№ 10789

SLf-UNet: Improved UNet for Brain MRI Segmentation by Combining Spatial and Low-Frequency Domain Features

Hui Ding, Jiacheng Lu, Junwei Cai, Yawei Zhang and Yuanyuan Shang

August 28, 2023

SLf-UNet: Improved UNet for Brain MRI Segmentation by Combining Spatial and Low-Frequency Domain Features*

Hui Ding[1,2][0000−0002−1920−7613](✉), Jiacheng Lu[1][0009−0002−7920−3814], Junwei Cai[1], Yawei Zhang[1], and Yuanyuan Shang[1,2]

[1] College of Information Engineering, Capital Normal University, Beijing, China
dhui@cnu.edu.cn
[2] Beijing Advanced Innovation Center for Imaging Technology, Beijing, China

Abstract. Deep learning-based methods have shown remarkable performance in brain tumor image segmentation. However, there is a lack of research on segmenting brain tumor lesions using frequency domain features of images. To address this gap, an improved network SLf-UNet has been proposed in this paper, which is a two-dimensional encoder-decoder architecture combining spatial and low-frequency domain features based on U-Net. The proposed model effectively learns information from spatial and frequency domains. Herein, we present a novel upsample approach by using zero padding in the high-frequency region and replacing the part of the convolution operation with a convolution block combining spatial frequency domain features. Our experimental results demonstrate that our method outperforms current mainstream approaches on BraTS 2019 and BraTS 2020 datasets.

Keywords: Frequency Analysis · BraTS · Image Segmentation.

1 Introduction

Medical image segmentation is a crucial tool for disease diagnosis, treatment planning, and follow-up services. In particular, brain MRI analysis often uses image segmentation to measure and visualize the regions and volumes of brain tumors. Since 2012, the Brain Tumor Segmentation (BraTS) Challenge has been held annually at MICCAI (Medical Image Computing and Computer Assisted Intervention). has become a leading benchmark in the field of medical image segmentation [1][2]. Gliomas are malignant brain tumors that vary in aggressiveness. Therefore, automated and accurate segmentation of these malignancies on magnetic resonance imaging (MRI) is essential for clinical diagnosis [3].

Automated medical image segmentation techniques have proven effective for accurately delineating brain tumors[4]. Recently, deep learning approaches [5][6][7][8] have achieved state-of-the-art performance for brain tumor segmentation on various benchmarks, owing to the powerful feature extraction of CNNs

* Supported by the National Natural Science Foundation of China (61876112).

[9]. The U-Net architecture [10], using an encoder-decoder structure with skip connections for detail retention, has become mainstream. UNet3+ [11] and UCTransnet [12] further improved UNet-like models by enhancing skip connections. The former employs full-scale connections for multi-scale feature fusion, while the latter adopts channel-wise attention for a more effective combination. Usually, three-dimensional (3D) deep learning frameworks would achieve higher accuracy in brain tumor segmentation tasks but encounter obstacles like a high computational burden. Facing these challenges, how to further optimize brain tumor segmentation models to improve segmentation accuracy remains an important issue [13][14].

Frequency analysis decomposes images into components, providing rich representations for more effective image understanding over spatial-only approaches [15]. In brain tumor images, tissue edges exhibit high-frequency changes, while lesions show gentle, low-frequency variations. Incorporating frequency domain analysis enhances lesion features and improves model feature extraction.

Based on frequency analysis, this paper proposed an improved network SLf-UNet, the following are the contributions of this work:

1) The proposed network, SLf-UNet, incorporates both spatial domain and low-frequency domain characteristics. And the impact of high and low-frequency components on segmentation was discussed and analyzed through experiments.

2) SF-block is proposed for effective fusion in the space-frequency domain. It utilizes both spatial and frequency information from feature maps to achieve information fusion.

3) For upsampling, we present a novel module zFUP, which solved the different scale matching between spatial and frequency domains in deep convolution layers by using zero-padding in the spectrum.

4) The proposed network structure achieves excellent performance on BraTS 2019 and BraTS 2020 datasets.

2 Related Works

While most research concentrates on model architectures, some recent work leverages frequency domain information to address medical imaging challenges using frequency transforms.

Stuchi et al. [16] enhanced image classification via frequency analysis. Luan et al. [17] used high-frequency filtering to enhance the edge and fine structure of breast images. Hu et al. [18] used high and low-pass filters for ultrasound thyroid segmentation. Li et al.[19] utilized wavelet transform in medical multispectral image fusion to exploit the frequency domain information of the images, which helps highlight features of the target area. Azad et al. [20] pointed out that vanilla CNNs tend to be biased towards textures while overlooking shape information for medical image segmentation. They proposed an adaptive frequency recalibration to reduce this bias and improve feature discrimination.

For brain tumor segmentation, Tang et al. proposed a novel model called tKFC-Net [21], which integrates spatial and frequency domain features via the

Fast Fourier Transform (FFT). However, it is worth noting that t-KFC incurs a high computational cost, and its adoption of high-frequency components renders it not necessary for brain tumor image segmentation. This limitation arises from the concentration of valuable information in the low-frequency region of brain tumor images, as will be verified in Section 4.5. Therefore, while the proposed tKFC-Net model demonstrates an innovative approach to incorporating frequency representations within CNNs, its limitations regarding computational efficiency and compatibility with brain tumor segmentation tasks warrant further investigation and optimization.

3 Method

In this paper, we proposed an improved frequency network, which combing the spatial and low-frequency convolution, and using the zero-padding to enhancement the up-sampling.

3.1 SLf-UNet

Fig. 1 illustrates the architecture of SLf-UNet, a 2D model for BraTS. This model is based on a U-Net encoder-decoder architecture that utilizes skip connections to combine high-level and low-level features. The key components of this model are the Spatial Frequency domain combining block (SF-block) and Zero-padding Upsampling Pyramid in Frequency Domain (zFUP).

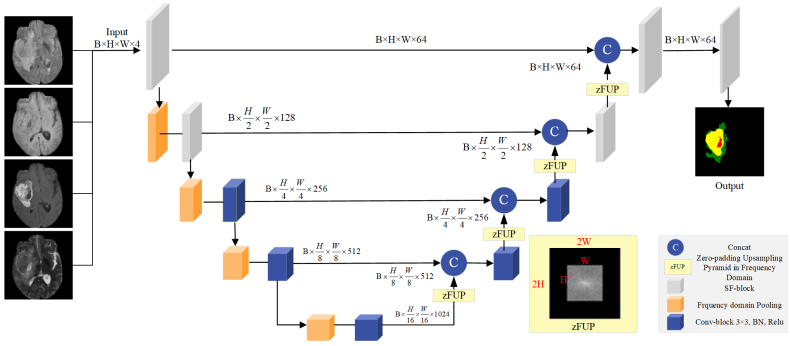

Fig. 1. The overall architecture of SLf-UNet. The architecture primarily comprises zFUP, SF-block, frequency domain pooling, while retaining the classical U-Net skeleton.

The input to the model consists of a series of 4-channel brain tumor slices. To enhance performance, we have incorporated the SF-Block in the first two layers of the encoder and the last two layers of the decoder to introduce low-frequency components and enable the model to learn effectively. However, applying SF-Blocks to all layers would significantly increase the computational cost. Moreover, as the number of layers deepens, the impact of introducing low-frequency

components diminishes. Hence, we have opted to use SF-Blocks in the first half of the encoder and its corresponding layers in the decoder. This approach strikes a balance between introducing low-frequency components and managing computational complexity. Additionally, we replaced all pooling methods with frequency domain pooling blocks and utilized ZFUP for upsampling to align features from different scales.

3.2 Spatial Frequency domain combining block (SF-block)

SF-block, which integrates both spatial and frequency domain features for CNNs in brain tumor segmentation. The module utilizes frequency domain information while preserving spatial cues. To analyze the influence of the two domains, we designed several optional branches in the structure (Fig. 2).

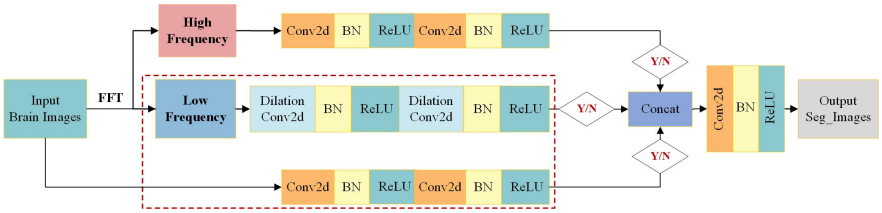

Fig. 2. Spatial and frequency domain Fourier convolution(SF-block). Three optional branches are given in the figure, namely the spatial branch, the low-frequency branch and the high-frequency branch. The influence of different components on the segmentation results is tested through different choices.

It first obtains high and low frequencies via a 2D discrete Fourier transform. Corresponding kernels then convolve the spatial features to generate spatial, low-frequency, and high-frequency branches. Features from the branches are combined before outputting.

Given spatial input $x \in R^{M \times N}$ with spectrum $X \in C^{M \times N}$, the low x^l and high x^h frequency components are obtained. These components and the original input x are then convolved with specific kernels as follows:

$$X = F(x) \quad x \in R^{M \times N}, X \in C^{M \times N} \tag{1}$$

where $F(\bullet)$denotes 2D-DFT, which transforms spatial feature x into spectral representation X. The components of low-frequency part and high-frequency part are as follows:

$$X_{mn}^{l} = \begin{cases} X_{mn} & \frac{M}{4} < m \leq \frac{3 \times M}{4}, \frac{N}{4} < n \leq \frac{3 \times N}{4} \\ 0 & \text{others} \end{cases} \tag{2}$$

$$X_{mn}^{h} = \begin{cases} 0 & \frac{M}{4} < m \leq \frac{3\times M}{4}, \frac{N}{4} < n \leq \frac{3\times N}{4} \\ X_{mn} & \text{others} \end{cases} \tag{3}$$

where X_{mn}^{l} denote low frequency part, X_{mn}^{h} denote high frequency part, and M and N denote the width and height of the feature map. Then transform the frequency parts back to spatial domain:

$$x^{l} = F^{-1}(X^{l}) \quad x^{l} \in R^{M\times N} \tag{4}$$

$$x^{h} = F^{-1}(X^{h}) \quad x^{h} \in R^{M\times N} \tag{5}$$

where x^{l} denotes spatial features of low frequency partes, and x^{h} denotes spatial features of high frequency partes, $F^{-1}(\bullet)$ denotes 2D-IDFT.

Fig. 3 demonstrates branching in the SF-block. As frequency components increase computation, the high-frequency section here contains less lesion information. Thus, removing this branch to eliminate irrelevant interference can facilitate lesion segmentation.

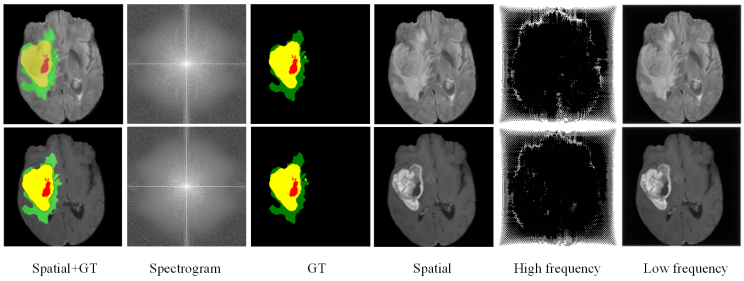

Fig. 3. Component examples in SF-block. The top and bottom rows present flair and t1ce modalities. Columns 4-6 are outputs of the spatial, high-frequency (binarized), and low-frequency branches respectively, with columns 1 and 3 displaying the corresponding ground truths and column 2 showing the spatial spectral image.

For the three branches, the original spatial feature branch and the high frequency branch adopts normal 3 × 3 kernel while the low frequency feature employs a dilated kernel with rate of 2, which benefits the smooth low frequency components and yields a broader sight vision. Then different branch combinations are selected, and lastly they are combined in series and input into the subsequent network structure:

$$x^{out} = concat(ax, bx^{l}, cx^{h}) \quad x^{out} \in R^{M\times N} \tag{6}$$

Here, a, b, and c are binary variables (1 being selected, 0 not selected) indicating the selection of three branches. This improved frequency domain convolution structure utilizes both spatial and frequency information, where the two complementary image cues produce refined features with rich semantics and details.

3.3 Zero-padding Upsampling Pyramid (zFUP)

UNet adopts an encoder-decoder framework to learn image features via convolutions. As the extracted feature maps are downsized, the decoder upsamples them to regain the original image sizes for final predictions. Common upsampling methods like deconvolution and bilinear interpolation directly enlarge feature maps. Although restoring the size and most information, they may introduce noise. Here, we recommend using zFUP - zero-padding for frequency-domain upsampling (Fig.4, and Fig.1 bottom right).

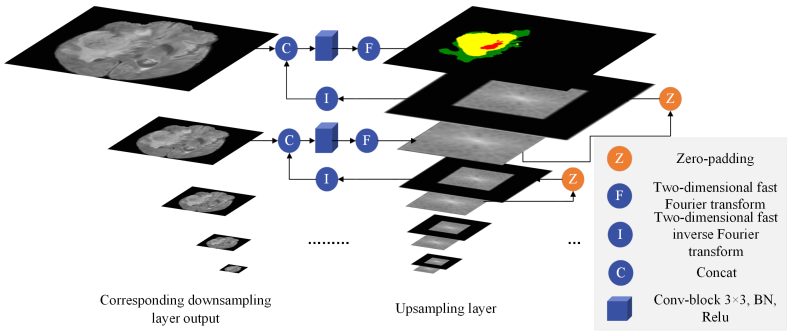

Fig. 4. Schematic diagram of zFUP. During the zFUP, each layer of input is combined with the output of the corresponding downsampling layer after zero/-padding to pass through the convolutional layer.

As Fig.3 shows and aforementioned, high-frequency components have minimal impacts whereas low-frequency ones greatly affect segmentation. Unlike zFUP, tKFC-Net's [21] upsampling divides the preceding output into low and high-frequency regions, generating padding results through a weighted approach. This allows the propagation of high-frequency information from the preceding layer to the low-frequency region of the subsequent layer. In contrast, the zFUP module directly takes the preceding output as the central part of the frequency domain for the next layer, applying zero-padding, and then concatenates it with the inverse-transformed spatial image. This strategy focuses the learning process on low-frequency features and optimizes computation by avoiding other padding techniques.

The proposed approach begins by subjecting the input feature map to a Fourier transform, converting it into the frequency domain. Subsequently, the spectrum is padded, doubling the size of each frequency dimension to simulate conventional pooling with a dilation rate of 2. We introduce adjustable padding with the same rate for frequency upsampling. Finally, the inverse transformation reconverts the data back to the spatial domain, resulting in an upsampled map of twice the original size.

3.4 Loss Function

In training, a hybrid loss function combining cross-entropy loss and Dice loss is adopted. The cross-entropy loss is defined as:

$$L_{bce} = -\sum_{i=1}^{W}\sum_{j=1}^{H}[T_{ij}\ \log(P_{ij}\ ) + (1 - T_{ij}\ )\ \log(1 - P_{ij}\ )\ ] \tag{7}$$

where W and H denote the width and height of the predicted image P_{ij} and the ground-truth image T_{ij}. And (i, j) are the coordinates of the pixels in the predicted image P_{ij} and the ground truth imageT_{ij}.

And the Dice loss is defined as:

$$L_{dice}(P, T) = 1 - 2 \times \frac{\sum_{i=1}^{N} p_i g_i + \tau}{\sum_{i=1}^{N} p_i + \sum_{i=1}^{N} g_i + \tau} \tag{8}$$

where summation is carried over the N voxels of the ground truth volume $t_i \in T$ and the predicted volume $p_i \in P$, and τ is a minimal constant to prevent division by zero.

Based on the above two loss functions, we propose a joint loss function composed of BCE and Dice:

$$L_{joint} = \sum_{i=1}^{3}(\lambda L_{dice_i} + (1 - \lambda)L_{bce_i}) \tag{9}$$

where λ is the weight to balance different losses, the value range is $0 < \lambda < 1$, and set to 1 in the experiment. In order to reduce the complexity of the task, we divide the task of segmenting the three-category lesion area into a single-category segmentation task with 3 channels, and calculate the loss separately. Where L_{dice_i} and L_{bce_i} represent the Dice loss and BCE loss of the i-th channel, respectively.

4 Experiments

4.1 Datasets

This paper utilizes BraTS 2019 and 2020 datasets, providing 3D MRI with voxel-wise ground truth labels annotated by physicians for evaluating state-of-the-art brain tumor segmentation methods [22][23][24]. BraTS 2019 contains 259 HGG and 76 LGG cases, while BraTS 2020 has 369 scans with more HGG cases. Each patient has four modalities: T1, T2, T1ce, and FLAIR MRI. Experts labeled the images into background, non-enhanced region, edema, and enhancing tumor based on unified standards. All scans have 240×240×155 voxel sizes. We focus on segmenting three regions: enhancing tumor for ET; whole tumor with ET + NET + ED; and tumor core containing ET + NET.

4.2 Pre-processing

The image contrast of the four modalities of the glioma image dataset is different, so the z-score method is used to normalize the images of each modality separately. The 1% highest and lowest intensities are removed, and subtracting the mean and dividing by the standard deviation of the intensities within the body. And after, cropping the size of images into $160 \times 160 \times 155$ to eliminate the unnecessary background. Then, obtained the slices of 3D brain tumor MRI images. In order to address the class imbalance problem, the slices without label pixels are excluded from trainset. Finally, the slices of the four modalities of the data are combined into multi-channel, and finally saved in npy for subsequent experiments.

4.3 Implementation Details

The experimental environment is: Ubuntu 18.04, NVIDIA GeForce GTX 2080Ti x1, Intel Core i7-4790k @ 4.00GHz quad-core CPU. And the experiment is based on the deep learning framework of Python 3.6 and Pytorch 1.6.0. We employed the Adam optimizer with an initial learning rate of 3e-4. Model regularization was conducted using L2 norm with a weight decay rate of 1e-4. For all models, we set the maximum number of training epochs to 500 and implemented early stopping after 50 epochs. Most models were terminated around 300 epochs during training. All models were implemented in Pytorch.

4.4 Evaluation Metrics

In this paper, we evaluate brain tumor segmentation using two widely used medical imaging metrics - Dice similarity coefficient (DSC) and Hausdorff distance (HD). DSC measures overlap and similarity between segmentation and ground truth. It weights recall and false positives equally. DSC is defined as:

$$DSC(P,T) = \frac{2|P_1 \cap T_1|}{|P_1| + |T_1|} \tag{10}$$

where P_1 is the predicted tumor region, T_1 is the true tumor region. DSC ranges from 0 to 1, higher values signify better segmentation.

Hausdorff distance (HD) evaluates structural differences between segmentation and truth. It is defined as:

$$Haus(T,P) = max\{sup_{t \in T} inf_{p \in P}, sup_{p \in P} inf_{t \in T} d(t,p)\} \tag{11}$$

where the inf and sup denote the lowest and highest distances, t and p are surfaces of the true and predicted regions, and $d(t,p)$ calculates distance between points t and p.

4.5 Ablation Study

To analyze the impacts of spatial and frequency domains, we conducted SLf-UNet with different channel settings (Table 1): solely spatial, solely low-frequency, solely high-frequency, and jointly spatial-low. Results in Table 1 show adding high-frequency channels decreased segmentation performance. Hence, we focused on exploring the synergistic effects of low-frequency and spatial channels.

Table 1. ABLATION STUDY ON BraTS 2019 DATASET.

Model	Dice_score(%)			Haussdorff95		
	ET↑	WT↑	TC↑	ET↓	WT↓	TC↓
SLf-UNet (spatial only)	86.23	**83.37**	84.74	1.6124	**2.6319**	1.6599
SLf-UNet (low frequency only)	86.14	83.35	85.35	1.6153	2.7217	1.6783
SLf-UNet (high frequency only)	54.25	61.30	58.99	2.5454	3.5946	2.6147
SLf-UNet (spatial and lowfrq, ours)	**87.61**	83.31	**86.86**	**1.5695**	2.7135	**1.6244**

Table 1 presents ablation results on BraTS 2019. Combining low-frequency and spatial channels yielded Dice scores of 87.61, 83.31, and 86.86 for ET, WT, and TC, outperforming other settings except WT. As Section 3.2 and Fig. 3 explain, low-frequencies contain most lesion information but lack whole tumor edge details, possibly contributing to the slight WT decrease. These results demonstrate incorporating spatial and low-frequency cues enhances SLf-UNet's effectiveness in segmenting medical images like BraTS.

4.6 Multi-method Comparison

Table 2 and 3 show the comparison of the brain tumor segmentation performance of our proposed Network SLf-UNet and the performance of other representative segmentation networks, included U-Net, UNet3+, UCTansNet, tKFC-Net, and transUNet.

Table 2. PERFORMANCE ON BraTS 2019 DATASET.

Model	Source	Dice_score(%)			Haussdorff95		
		ET↑	WT↑	TC↑	ET↓	WT↓	TC↓
U-Net	2015 MICCAI	77.10	84.06	84.50	-	-	-
UNet 3+	2020 ICASSP	87.04	83.48	86.06	1.5654	**2.6372**	1.6306
tKFC-Net	2021 CMPB	78.15	**84.57**	86.52	-	-	-
TransUNet	2021arxiv	80.69	80.74	77.23	1.7599	2.7598	1.8783
UCTransnet	2022 AAAI	84.99	84.32	83.43	1.5951	2.6471	1.7347
SLf-UNet(our)		**87.61**	83.31	**86.86**	**1.5695**	2.7135	**1.6244**

For BraTS'19, 285 subjects were used for training and 50 for testing. After preprocessing, the dataset had 15,138 images for training, 3,785 for validation

and 3,219 for testing. Table 2 evaluates segmentation of WT, TC and ET using the mentioned metrics. In the BraTS'20 experiment, the 369 subjects in the dataset were divided into training and test sets at a 8:2 ratio. The preprocessed slices were evaluated, including ground-truths.

Table 3. PERFORMANCE ON BraTS 2020 DATASET.

Model	Source	Dice_score(%)			Haussdorff95		
		ET↑	WT↑	TC↑	ET↓	WT↓	TC↓
U-Net	2015 MICCAI	90.87	86.3	87.76	0.6813	1.3916	0.9049
UNet3+	2020 ICASSP	91.53	87.35	88.61	0.6781	1.3207	0.8903
TransUNet	2021arxiv	89.75	84.01	86.81	0.7272	1.4253	0.9507
UCTransnet	2022 AAAI	90.37	**88.18**	88.56	0.6971	**1.2707**	0.9063
SLf-UNet (ours)		**91.83**	87.62	**88.94**	**0.6662**	1.3166	**0.8873**

Table 3 compares SLf-UNet with other networks. The experimental results in Tables 2-3 demonstrate that the improved SLf-UNet achieves comparable WT segmentation performance to other networks, while attaining higher accuracy on ET and TC. On BraTS 2019, SLf-UNet obtained Dice scores of 87.61, 83.31, 86.86 for ET, WT, TC respectively; and HD95 values of 1.5695, 2.7135, 1.6244 respectively. On BraTS 2020, it achieved Dice scores of 91.83, 87.62, 88.94; and HD95 values of 0.6662, 1.3166, 0.8873 respectively. Fig. 5 presents SLf-UNet segmentation outputs and multi-modal examples. As shown, the segmentation results exhibit improved effects on details and edges.

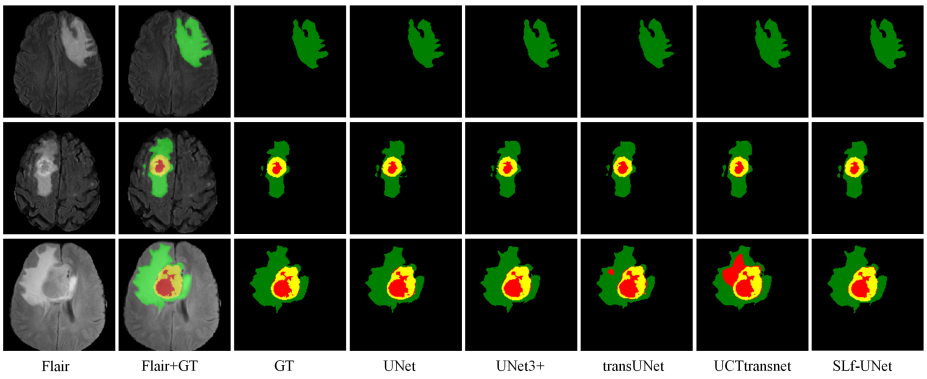

Fig. 5. Examples of Multi-method segmentation results. For the segmentation result image, where Green: peritumoral edematous/invaded tissue, red: necrotic tumor core, yellow: GD-enhancing tumor.

5 Conclusion

We propose a novel 2D multi-modal spatial-frequency segmentation algorithm for brain tumor MRI, validated on BraTS 2019 and 2020. Experiments show our network outperforms most cutting-edge methods. The core innovation is incorporating frequency domain information through adaptive Fourier transforms, learnable convolution kernels, and an efficient upsampling module zFUP. Future work will explore advanced frequency integration techniques to further improve tumor segmentation and broader medical image analysis.

References

1. Withey, D., Koles, Z.: Three generations of medical image segmentation: Methods and available software. International Journal of Bioelectromagnetism **9**, 67–68 (2007)
2. Lai, M.: Deep learning for medical image segmentation. arXiv preprint arXiv:1505.02000 (2015)
3. Wang, W., Chen, C., Ding, M., Yu, H., Zha, S., Li, J.: Transbts: Multimodal brain tumor segmentation using transformer. In: Medical Image Computing and Computer Assisted Intervention–MICCAI 2021. pp. 109–119. Springer (2021)
4. Huo, Y., Xu, Z., Xiong, Y., Aboud, K., Parvathaneni, P., Bao, S., Bermudez, C., Resnick, S.M., Cutting, L.E., Landman, B.A.: 3d whole brain segmentation using spatially localized atlas network tiles. NeuroImage **194**, 105–119 (2019)
5. Isensee, F., Jager, P.F., Full, P.M., Vollmuth, P., Maier-Hein, K.H.: nnu-net for brain tumor segmentation. In: Brainlesion: Glioma, Multiple Sclerosis, Stroke and Traumatic Brain Injuries. pp. 118–132. Springer (2020)
6. Jiang, Z., Ding, C., Liu, M., Tao, D.: Two-stage cascaded u-net: 1st place solution to BraTS challenge 2019 segmentation task. In: Brainlesion: Glioma, Multiple Sclerosis, Stroke and Traumatic Brain Injuries. pp. 231–241. Springer (2019)
7. Milletari, F., Navab, N., Ahmadi, S.A.: V-net: Fully convolutional neural networks for volumetric medical image segmentation. In: fourth international conference on 3D vision (3DV). pp. 565–571. IEEE (2016)
8. Bischke, B., Helber, P., Folz, J., Borth, D., Dengel, A.: Multi-task learning for segmentation of building footprints with deep neural networks. In: IEEE International Conference on Image Processing (ICIP). pp. 1480–1484. IEEE (2019)
9. Hatamizadeh, A., Nath, V., Tang, Y., Yang, D., Roth, H.R., Xu, D.: Swin unetr: Swin transformers for semantic segmentation of brain tumors in mri images. In: Brainlesion: Glioma, Multiple Sclerosis, Stroke and Traumatic Brain Injuries. pp. 272–284. Springer (2021)
10. Ronneberger, O., Fischer, P., Brox, T.: U-net: Convolutional networks for biomedical image segmentation. In: Medical Image Computing and Computer-Assisted Intervention–MICCAI 2015. pp. 234–241. Springer (2015)
11. Huang, H., Lin, L., Tong, R., Hu, H., Zhang, Q., Iwamoto, Y., Han, X., Chen, Y.W., Wu, J.: Unet 3+: A full-scale connected unet for medical image segmentation. In: IEEE International Conference on Acoustics, Speech and Signal Processing (ICASSP). pp. 1055–1059. IEEE (2020)
12. Wang, H., Cao, P., Wang, J., Zaiane, O.R.: Uctransnet: rethinking the skip connections in u-net from a channel-wise perspective with transformer. In: Proceedings of the AAAI conference on artificial intelligence. pp. 2441–2449. AAAI Press (2022)

13. Liu, X., Song, L., Liu, S., Zhang, Y.: A review of deep-learning-based medical image segmentation methods. Sustainability **13**, 1224 (2021)
14. Hesamian, M.H., Jia, W., He, X., Kennedy, P.: Deep learning techniques for medical image segmentation: achievements and challenges. Journal of digital imaging **32**, 582–596 (2019)
15. Brosch, T., Tam, R.: Efficient training of convolutional deep belief networks in the frequency domain for application to high-resolution 2d and 3d images. Neural computation **27**, 211–227 (2015)
16. Stuchi, J.A., Angeloni, M.A., Pereira, R.F., Boccato, L., Folego, G., Prado, P.V., Attux, R.R.: Improving image classification with frequency domain layers for feature extraction. In: IEEE 27th International Workshop on Machine Learning for Signal Processing (MLSP). pp. 1–6. IEEE (2017)
17. Luan M, Cui G, S.W.: Mammogram image enhancement method based on power-law transformation and high frequency emphasis filtering. Journal of Bohai University(Natural Science Edition) pp. 40(04):378–384 (2019)
18. Hu, Y., Qin, P., Zeng, J., Chai, R., Wang, L.: Ultrasound thyroid segmentation based on segmented frequency domain and local attention. Journal of Image and Graphics **25**, 2195–2205 (2020)
19. Li, J., Chen, C., Wang, L.: Fusion algorithm of multi-spectral images based on dual-tree complex wavelet transform and frequency-domain u-net. Journal of Biomedical Engineering Research **39**, 145–150 (2020)
20. Azad, R., Bozorgpour, A., Asadi-Aghbolaghi, M., Merhof, D., Escalera, S.: Deep frequency re-calibration u-net for medical image segmentation. In: Proceedings of the IEEE/CVF International Conference on Computer Vision. pp. 3274–3283. IEEE (2021)
21. Tang, X., Peng, J., Zhong, B., Li, J., Yan, Z.: Introducing frequency representation into convolution neural networks for medical image segmentation via twin-kernel fourier convolution. Computer Methods and Programs in Biomedicine **205**, 106110 (2021)
22. Menze, B.H., Jakab, A., Bauer, S., Kalpathy-Cramer, J., Farahani, K., Kirby, J., Burren, Y., Porz, N., Slotboom, J., Wiest, R.: The multimodal brain tumor image segmentation benchmark (BraTS). IEEE transactions on medical imaging **34**, 1993–2024 (2014)
23. Bakas, S., Akbari, H., Sotiras, A., Bilello, M., Rozycki, M., Kirby, J.S., Freymann, J.B., Farahani, K., Davatzikos, C.: Advancing the cancer genome atlas glioma mri collections with expert segmentation labels and radiomic features. Scientific data **4**, 1-13 (2017)
24. Bakas, S., Reyes, M., Jakab, A., Bauer, S., Rempfler, M., Crimi, A., Shinohara, R.T., Berger, C., Ha, S.M., Rozycki, M.: Identifying the best machine learning algorithms for brain tumor segmentation, progression assessment, and overall survival prediction in the BraTS challenge. arXiv preprint arXiv:1811.02629 (2018)